

A Novel Method for Low-Contrast and High-Noise Vessel Segmentation and Location in Venipuncture

Yuhe Li, Zhendong Qiao, Shaoqin Zhang, Zhenhuan Wu, Xueqin Mao, Jiahua Kou, and Hong Qi

Abstract—Blood sampling is the most common medical technique, and vessel detection is of crucial interest for automated venipuncture systems. In this paper, we propose a new convex-regional-based gradient model that uses contextually related regional information, including vessel width size and gray distribution, to segment and locate vessels in a near-infrared image. A convex function with the interval size of vessel width is constructed and utilized for its edge-preserving superiority. Moreover, white and linear noise independences are derived. The region-based gradient decreases the number of local extreme in the cross-sectional profile of the vessel to realize its single global minimum in a low-contrast, noisy image. We demonstrate the performance of the proposed model via quantitative tests and comparisons between different methods. Results show the advantages of the model on the continuity and smoothness of segmented vessel. The proposed model is evaluated with receiver operating characteristic curves, which have a corresponding area under the curve of 88.8%. The proposed model will be a powerful method in automated venipuncture system and medical image analysis.

Index Terms—Vessel segmentation, regional-gradient, noise independence, convex function optimization, venipuncture system.

I. INTRODUCTION

MOST medical treatments depend on the important phase of medication or blood sampling in which trained medical staff locate the best veins either by sight or by palpation in difficult cases. Venipuncture and intravenous catheterization procedures are performed billions of times annually in hospitals, clinics, and laboratories. Even skilled medical practitioners, however, find vein localization difficult given the different physiological characteristics of patients, such as darker skin tones, scars, vein depth, hairiness, or dehydration. The difficulty in vein localization increases the number of attempts at venipuncture, thus causing unnecessary pain, anxiety, skin bruising, vein damage, or even life-threatening

infections [1]. Some vein-imaging systems have been developed with near-infrared (NIR) technology to improve the success rate of venipuncture [2]. NIR is widely accepted in biomedical applications because of its non-invasiveness for subcutaneous vein localization. Currently, some research groups are developing an optimal device that uses NIR imaging to localize veins and ultrasound to confirm blood flow in the selected vein [3].

Vessel image segmentation is a crucial step in clinical tasks and provides information about the relative size, shape, and orientation of blood vessels. Most proposed segmentation methods are based on the assumption that vascular objects, such as subcutaneous veins, can be conceptualized anatomically as hollow tube structures with different orientations and scales [4]. Various segmentation methods have been proposed in the past decades [5]–[8]. Segmentation algorithms are based on one of the two properties of gray values for monochrome vessel images: discontinuity and similarity. Discontinuity segmentation partitions an image on the basis of abrupt changes in gray-scale levels, whereas similarity segmentation is based on thresholding and regional operations [9]. Existing vessel segmentation methods with different objectives are divided into two categories: surface segmentation and skeleton segmentation [10], [11]. Various filters, such as Canny detector, have been proposed [12], [13]. Vessel segmentation techniques can also be categorized as either supervised or unsupervised segmentation based on overall system design and architecture. Supervised segmentation utilizes training data to train a classifier, such as Gaussian mixture models [14], k-nearest neighbors [15], and support vector machine [16]. By contrast, unsupervised segmentation does not require training data. The lower requirement for data and training makes unsupervised methods more applicable for a wider range of imaging modalities. This category comprises most segmentation techniques in the literature [17], [18], including the proposed method in this paper. For geometrically curve-like structures a new kind of approach termed minimal path propagation with backtracking (MPP-BT), is proposed to improve the centerline extraction performance [19]. The MPP-BT approach makes full use of the information in the process of backtracking to overcome some problems commonly encountered in the application of minimal path tracking method, such as endpoint, shortcut and accumulation problems.

Image segmentation remains a widely studied and largely unsolved problem in medical image processing. For example,

Manuscript received May 4, 2017; revised June 20, 2017; accepted July 20, 2017. Date of publication July 27, 2017; date of current version October 25, 2017. (Corresponding author: Yuhe Li.)

Y. Li, Z. Qiao, Z. Wu, and J. Kou are with the Department of Precision Instrument, Tsinghua University, Beijing 100084, China (e-mail: liyuhe@mail.tsinghua.edu.cn; thubofu@126.com; 83166192@qq.com; kjh72@126.com).

S. Zhang, X. Mao, and H. Qi are with the Haidian Maternal Child Health Hospital, Beijing 100080, China (e-mail: m13661299372@163.com; bluemxq@sina.com; qihong2008@sina.com).

Color versions of one or more of the figures in this paper are available online at <http://ieeexplore.ieee.org>.

Digital Object Identifier 10.1109/TMI.2017.2732481

accurately locating veins that are not obvious, such as in newborns, children, obese people, and certain diseases, is difficult even by a skilled nurse or NIR imaging system. Studies have shown that the effectiveness of NIR imaging likely depends on physiological parameters, including skin melanin concentration, skin thickness, vessel wall interfaces, and the combined effects of vein depth and diameter [20]. The most intuitive segmentation technique is simple differencing followed by thresholding. Change is detected if the difference in gray levels between the neighboring pixels exceeds a preset threshold. As a result, both the computational cost and complexity of this technique are low, but is highly sensitive to noise or blurring. Hence, it is unsuitable for environments with low contrast and high noise. For low-dose medical images some pre- and post-processing algorithms are applied to reduce the noise and residual artifacts by using fast Dictionary Learning (DL) and Weighted Intensity Averaging over Large-scale Neighborhoods (WIA-LN) [21]–[23]. Segmentation approaches that are based on intensity distributions at the regional level work well in noisy environments, but they are sensitive to changes in illumination because they only employ intensity difference measures [24]. Non-uniform illumination may change the histogram of the vessel image; hence, segmenting an image with a single local threshold becomes impossible.

We present a novel method that: overcomes the difficulty in segmentation and location of low-contrast, noisy vein images; coordinates with the system development of automated, image-guided venipuncture; and increases first-stick accuracy in medical treatments. The proposed method is based on the newly proposed convex-regional-based gradient (CRG) algorithm and fully exploits the regional, statistical analysis of vessel image and local thresholding. Moreover, the method simultaneously prevents over-segmentation with global minima in anatomically selective regions. The regional gradients of the vessel image are adopted to overcome the limitations caused by noise, non-uniform illumination, and blur. Experiments on both actual forearm and hand images demonstrate that the proposed CRG algorithm suppresses noise in the vessel region while retaining edge information. The final goal is to locate the vein to ease clinical parameter measurement and facilitate automated venipuncture device planning.

The rest of this paper is structured as follows. Section II provides the theoretical analysis of the mathematical model, noise independence, and edge extraction process, with special focus on the proposed CRG algorithm. Section III presents our experimental results, which were obtained on the center line and edges of vessels. To demonstrate the performance, accuracy, and robustness of the CRG algorithm, Section VI concludes this paper with a discussion on the following vessel modes: “Convex” and “Step,” receiver operating characteristic (ROC) curves, directivity, complexity analysis, and parameter initialization.

II. THEORETICAL ANALYSIS

A. Working Principle

Fig. 1 shows the schematic illustration of NIR image analysis for automated venipuncture. With respect to system design

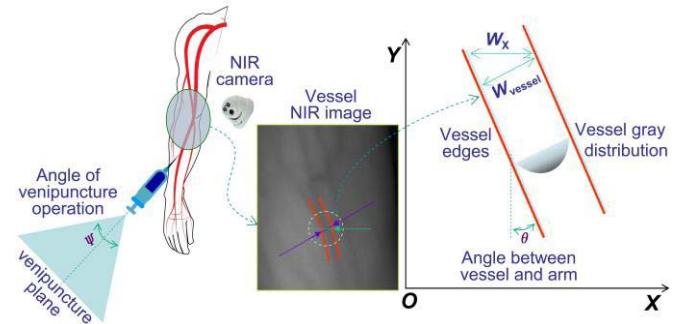


Fig. 1. Schematic illustration of vessel image analysis for automated venipuncture.

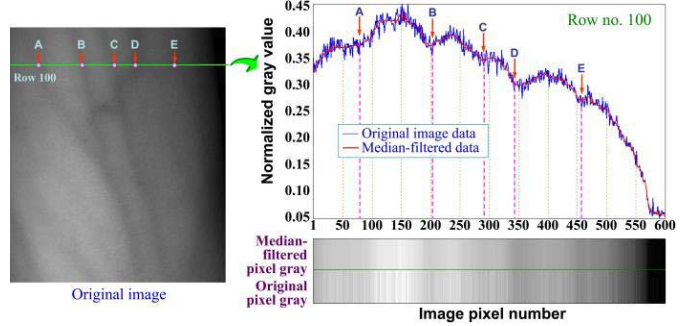


Fig. 2. Cross-sectional gray-level profile of row number 100.

and architecture, the direction of vessel used for puncture is along the length direction of the arm or hand. Here we assume that the arm is in the XOY plane, and the venipuncture plane of needle makes an angles of about 10 to 45 degrees with the XOY plane. As shown in Fig. 1, the Y-axis represents the direction of the arm and θ , W_X , W_{vessel} theoretically denote the angle between the vessel and the arm, the real width of the vessel, and the equivalent width of the vessel in X-axis direction, respectively. Then, we can obtain

$$W_X = W_{\text{vessel}} / \cos(\theta) \quad (1)$$

The selected vessel satisfies the condition $\theta \leq \psi/2$, ψ , which denotes the operation angle in venipuncture plane. Considering both the space occupied by the mechanical parts of the venipuncture device and the direction of the vessel in the arm or hand, ψ is designed to be less than 40° , then $\theta < 20^\circ$, $W_X < 1.06 W_{\text{vessel}}$. Thus, the relative difference between the equivalent and actual width can be neglected systematically. The NIR camera obtains the original image of the vessel. The calibrated one-pixel width Δx on the image plane in X-axis direction is approximately equal to 0.1 mm per pixel. The information on vessel segmentation and edge location is used to determine the optimal working angle of the venipuncture system.

B. Mathematical Model

To simplify calculation, the original grayscale image is normalized to the interval [0, 1]. Fig. 2 shows the cross-sectional profile of row number 100 along the X direction. The capital letters (A, B, C, and so on.) denote the center position of the vessel. The blue curve represents the original gray value of pixels on row number 100 and the red line

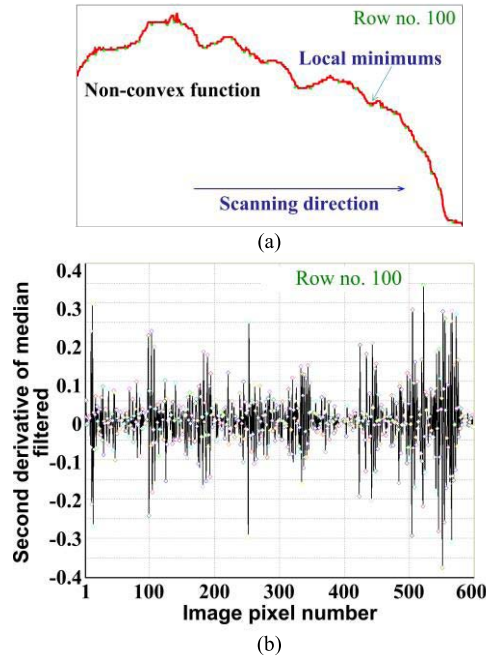


Fig. 3. Median-filtered image analysis. (a) median-filtered data; (b) second derivative.

represents the median-filtered data. Note that the pixel gray values of the vessel center do not necessarily coincide with the global minimum of any row because of external factors, such as non-uniform illumination and arm surface curvature.

The center axis of the vessel has a lower gray variation rate than other sections, as shown in Fig. 3(a). The green circle points correspond to the stationary points of the median-filtered curve. The scanline profile is fitted by a median filter to estimate the central points, edge locations, and direction of all the local vessels. A one-to-one correspondence between the stationary points and the locations of the vessel center does not exist. The method, which is based on the second derivative, analyzes the edges of the vessel, such as zero crossings of the second derivative. However, low-contrast, noisy images may be difficult to analyze. Although the image has been filtered, it is difficult to extract effective vessel information via the simple and direct method of the second derivative (Fig. 3(b)). Fig. 3(a) shows that the gray-level curve along the scanning direction (X-axis) is not a convex or concave function. Moreover, numerous local minima are present. An easy optimization method to guarantee global convergence for image segmentation and edge location does not exist for the non-convex function. For instance, if the central point in a 3×3 or 5×5 pixel sub-neighborhood of uniform grayscale has a zero gradient, all of the neighbors of the whole region must be examined to determine the correspondence of a sub-neighborhood to a local maximum or minimum [25].

We now assume that $x_{\text{vessel_center}}$ and δ_{vessel} numerically denote the center position and width (unit: mm) of the vessel in the X direction, respectively. The maximal diameter of the vessel is less than 3 mm, as shown in the NIR image in Fig. 1. Here, we take an initial value of $\delta_{\text{vessel}} = 3$ mm; correspondingly, the pixel number of the vessel along its width is $N_V = \delta_{\text{vessel}}/\Delta x = 30$ pixels. Finite difference approximation

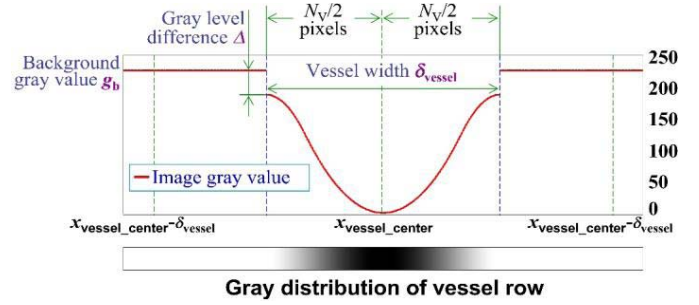


Fig. 4. Simplified centrosymmetric model of vessel in NIR image.

is the simplest method for estimating the derivative for the numerical analysis of an image that includes segmentation. These methods include three-point stencil for the first or second derivative. Usually, the maximum number of nodes for a compact stencil is 3 or 9. Take 3 as the pixel number for calculation to solve the first or second derivative. We set the edge interval of the vessel as $\mathbf{R}_{\text{vessel}} = [x_{\text{vessel_center}} - \delta_{\text{vessel}}/2, x_{\text{vessel_center}} + \delta_{\text{vessel}}/2]$. The pixel number used for the derivative accounted for 10% ($3/30 = 0.1$) of the interval length of the vessel. Additionally, the simple derivative operation can theoretically represent only the local features of the vessel, which may be difficult for low-contrast, noisy NIR images.

We focus on three hypotheses for simplicity: (1) The fitted curve across the vessel is approximately convex. (2) The vessel is implicitly assumed as a tubular structure that is symmetrical to the vessel centerline [26]. (3) The background has the same gray value g_b that is greater than or equal to the maximal gray value of the vessel, i.e., the gray level difference $\Delta \geq 0$. A simplified centrosymmetric model was built based on the physiological features of the vessel, as shown in Fig. 4.

The above model can be expressed in terms of a function:

$$f(x) = \begin{cases} g_b & x < x_{\text{vessel_center}} - \delta_{\text{vessel}}/2 \\ f_{\text{vessel}}(x) & x \in \mathbf{R}_{\text{vessel}} \\ g_b & x > x_{\text{vessel_center}} + \delta_{\text{vessel}}/2 \end{cases} \quad (2)$$

where $f_{\text{vessel}}(x)$ is a symmetrical smooth function with respect to the center position of vessel $x_{\text{vessel_center}}$. For any points x_1, x_2 of the closed interval $\mathbf{R}_{\text{vessel}}$, if the inequality $|x_1 - x_{\text{vessel_center}}| \geq |x_2 - x_{\text{vessel_center}}|$ holds, then we have $f_{\text{vessel}}(x_1) \geq f_{\text{vessel}}(x_2)$.

The inability to accurately detect edges in noisy environments limits traditional image operators. This problem is alleviated by extending the neighborhoods over areas where differential gradients are computed. Thus, the edge interval of vessel $\mathbf{R}_{\text{vessel}}$ is used instead of the three-point or five-point stencils to perform gradient calculation for the vessel image to segment and locate the vessel by overall features. The edge interval is more contextually meaningful, which accounts for all the pixels in the interval $\mathbf{R}_{\text{vessel}}$, compared with the traditional gradient neighborhood.

A CRG algorithm is proposed based on the regional differential geometry of the vessel. The term ‘‘convex’’ is borrowed from mathematical ‘‘convex function’’, which has many advantages for modeling and analysis. The CRG algorithm is the difference between the sum of gray values in an interval with width N_V that is centered over the pixel being processed,

and the sum of gray values in its left and right intervals with width $N_V/2$. The expression of CRG model function $F(x)$ can be given as follows:

$$F(x) = \sum_{n=0}^{N_V/2} (f(x+n\Delta x) + f(x-n\Delta x)) - \sum_{n=N_V/2+1}^{N_V+1} (f(x+n\Delta x) + f(x-n\Delta x)) \quad (3)$$

Next, we will further deduce the convexity of function $F(x)$.

$$\begin{aligned} F(x+\Delta x) - F(x) &= \left\{ \sum_{n=0}^{N_V/2} (f(x+\Delta x+n\Delta x) + f(x+\Delta x-n\Delta x)) - \sum_{n=N_V/2+1}^{N_V+1} (f(x+\Delta x+n\Delta x) + f(x+\Delta x-n\Delta x)) \right\} \\ &\quad - \left\{ \sum_{n=0}^{N_V/2} (f(x+n\Delta x) + f(x-n\Delta x)) - \sum_{n=N_V/2+1}^{N_V+1} (f(x+n\Delta x) + f(x-n\Delta x)) \right\} \\ &= \sum_{n=0}^{N_V/2} [f(x+(n+1)\Delta x) - f(x+n\Delta x)] \\ &\quad + \sum_{n=0}^{N_V/2} [f(x-(n-1)\Delta x) - f(x-n\Delta x)] \\ &\quad + \sum_{n=N_V/2+1}^{N_V+1} [f(x+n\Delta x) - f(x+(n+1)\Delta x)] \\ &\quad + \sum_{n=N_V/2+1}^{N_V+1} [f(x-n\Delta x) - f(x-(n-1)\Delta x)] \\ &= S_A + S_B + S_C + S_D \end{aligned} \quad (4)$$

where

$$\begin{cases} S_A = \sum_{n=0}^{N_V/2} [f(x+(n+1)\Delta x) - f(x+n\Delta x)] \\ \quad = f\left(x + \left(\frac{N_V}{2} + 1\right)\Delta x\right) - f(x) \\ S_B = \sum_{n=0}^{N_V/2} [f(x-(n-1)\Delta x) - f(x-n\Delta x)] \\ \quad = f(x+\Delta x) - f\left(x - \frac{N_V}{2}\Delta x\right) \\ S_C = \sum_{n=N_V/2+1}^{N_V+1} [f(x+n\Delta x) - f(x+(n+1)\Delta x)] \\ \quad = f\left(x + \left(\frac{N_V}{2} + 1\right)\Delta x\right) - f(x+(N_V+2)\Delta x) \\ S_D = \sum_{n=N_V/2+1}^{N_V+1} [f(x-n\Delta x) - f(x-(n-1)\Delta x)] \\ \quad = f(x-(N_V+1)\Delta x) - f\left(x - \frac{N_V}{2}\Delta x\right) \end{cases} \quad (5)$$

Then, we can obtain:

$$\begin{aligned} F(x+\Delta x) - F(x) &= 2 \left[f\left(x + \left(\frac{N_V}{2} + 1\right)\Delta x\right) - f\left(x - \frac{N_V}{2}\Delta x\right) \right] \\ &\quad + [f(x+\Delta x) - f(x)] \\ &\quad + [f(x-(N_V+1)\Delta x) - f(x+(N_V+2)\Delta x)] \end{aligned} \quad (6)$$

Substituting $N_V = \delta_{\text{vessel}}/\Delta x$ into formula (6) yields another expression:

$$\begin{aligned} F(x+\Delta x) - F(x) &= 2 \left[f\left(x + \frac{\delta_{\text{vessel}}}{2} + \Delta x\right) - f\left(x - \frac{\delta_{\text{vessel}}}{2}\right) \right] \\ &\quad + [f(x+\Delta x) - f(x)] \\ &\quad + [f(x-\delta_{\text{vessel}}-\Delta x) - f(x+\delta_{\text{vessel}}+2\Delta x)] \\ &= 2\Delta F_1 + \Delta F_2 + \Delta F_3 \end{aligned} \quad (7)$$

where

$$\begin{cases} \Delta F_1 = f(x+\delta_{\text{vessel}}/2+\Delta x) - f(x-\delta_{\text{vessel}}/2) \\ \Delta F_2 = f(x+\Delta x) - f(x) \\ \Delta F_3 = f(x-\delta_{\text{vessel}}-\Delta x) - f(x+\delta_{\text{vessel}}+2\Delta x) \end{cases} \quad (8)$$

Considering formula (2) and Fig. 4, when x belongs to the interval $[x_{\text{vessel_center}}, x_{\text{vessel_center}} + \delta_{\text{vessel}}/2]$, we can obtain: $\Delta F_1 = g_b - f\left(x - \frac{\delta_{\text{vessel}}}{2}\right) > 0$, $\Delta F_2 > 0$, and $\Delta F_3 = g_b - g_b = 0$; thus,

$$F(x+\Delta x) - F(x) = 2 \left[g_b - f\left(x - \frac{\delta_{\text{vessel}}}{2}\right) \right] + [f(x+\Delta x) - f(x)] > 0 \quad (9)$$

Similarly, when $x \in [x_{\text{vessel_center}} - \delta_{\text{vessel}}/2, x_{\text{vessel_center}}]$, the inequality $F(x+\Delta x) - F(x) < 0$ holds. For the interval $\mathbf{R}_{\text{vessel}}$, $F(x_{\text{vessel_center}})$ is the global minimum of CRG function $F(x)$, $F_{\min} = F(x_{\text{vessel_center}}) = \min(F(x))$. From a mathematical perspective, the CRG function $F(x)$ is a convex function that is defined on interval $\mathbf{R}_{\text{vessel}}$. The CRG function has a local minimum that is always a global minimum and its first derivative is increasing or at least non-decreasing. All these properties can be adopted in segmenting and locating the vessel. Conversely, using convex optimization methods with approximate convex function $f(x)$ does not always assure global approximation, especially for low-contrast, noisy images. Fig. 4 indicates that $x_{\text{vessel_center}}$ is at the center position of the vessel. Correspondingly, the minimum F_{\min} of $F(x)$ can be utilized for vessel segmentation and location. Moreover, the minimum F_{\min} is independent of white noise and linear noise.

C. White Noise Independence

For any point x in the interval $[x_{\text{vessel_center}}, x_{\text{vessel_center}} + \delta_{\text{vessel}}/2]$ (the rest may be deduced by analogy), we can obtain the following expression from formulae (7) and (8):

$$\begin{aligned} F(x+n\Delta x) - F(x) &= \{F(x+n\Delta x) - F(x+(n-1)\Delta x)\} \\ &\quad + \{F(x+(n-1)\Delta x) - F(x+(n-2)\Delta x)\} \\ &\quad \vdots \\ &\quad + \{F(x+2\Delta x) - F(x+\Delta x)\} + \{F(x+\Delta x) - F(x)\} \end{aligned}$$

$$= 2 \left[n g_b - \sum_{k=0}^{n-1} f(x + k \Delta x - N_V/2 \Delta x) \right] + f(x + n \Delta x) - f(x) \quad (10)$$

where the integer n ranges in value from 0 to $N_V/2$.

White noise $r(x)$ in magnitude images is commonly described by a distribution with the mathematical expectation μ and variance σ^2 ($\sigma^2 \neq 0$). Moreover, white noise is assumed to be independent of brightness [24]. On the basis of formula (3), we can obtain the CRG function $R(x)$ of white noise $r(x)$ as:

$$R(x) = \sum_{n=0}^{N_V/2} (r(x + n \Delta x) + r(x - n \Delta x)) - \sum_{n=N_V/2+1}^{N_V+1} (r(x + n \Delta x) + r(x - n \Delta x)) \quad (11)$$

Further deductions are given by:

$$\begin{aligned} & R(x + \Delta x) - R(x) \\ &= 2 \left[r\left(x + \left(\frac{N_V}{2} + 1\right) \Delta x\right) - r\left(x - \frac{N_V}{2} \Delta x\right) \right] \\ &+ [r(x + \Delta x) - r(x)] + [r(x - (N_V + 1) \Delta x) - r(x + (N_V + 2) \Delta x)] \end{aligned} \quad (12)$$

$$\begin{aligned} & R(x + n \Delta x) - R(x) \\ &= \{R(x + n \Delta x) - R(x + (n-1) \Delta x)\} \\ &+ \{R(x + (n-1) \Delta x) - R(x + (n-2) \Delta x)\} \\ &\vdots \\ &+ \{R(x + 2 \Delta x) - R(x + \Delta x)\} + \{R(x + \Delta x) - R(x)\} \\ &= 2 \left[\sum_{k=0}^{n-1} r(x + (N_V/2 + k + 1) \Delta x) - \sum_{k=0}^{n-1} r(x - (N_V/2 - k) \Delta x) \right] + [r(x + n \Delta x) - r(x)] \\ &+ \left[\sum_{k=0}^{n-1} r(x - (N_V - k + 1) \Delta x) - \sum_{k=0}^{n-1} r(x + (N_V + k + 2) \Delta x) \right] \\ &= 2 \Delta R_1 + \Delta R_2 + \Delta R_3 \end{aligned} \quad (13)$$

Assuming that the amplitude of the white noise is A_{noise} , then the inequality $\Delta R_2 \leq 2A_{\text{noise}}$ holds. Meanwhile, ΔR_1 and ΔR_3 can be transformed into the following expressions:

$$\begin{aligned} \Delta R_1 &= \sum_{k=0}^{n-1} r(x + (N_V/2 + k + 1) \Delta x) - \sum_{k=0}^{n-1} r(x - (N_V/2 - k) \Delta x) \\ &= \sum_{k=0}^{n-1} [r(x + (N_V/2 + k + 1) \Delta x) - r(x - (N_V/2 - k) \Delta x)] = \sum_{k=0}^{n-1} (\delta R_{1k}) \end{aligned} \quad (14)$$

$$\begin{aligned} \Delta R_3 &= \left[\sum_{k=0}^{n-1} r(x - (N_V - k + 1) \Delta x) - \sum_{k=0}^{n-1} r(x + (N_V + k + 2) \Delta x) \right] = \sum_{k=0}^{n-1} (\delta R_{3k}) \end{aligned} \quad (15)$$

where both δR_{1k} and δR_{3k} represent the sum of the difference between two equal length segments of the same white noise data. According to the Lindeberg-Levy central limit theorem (CLT), both $(\Delta R_1 - n\mu_1)/\sqrt{n}\sigma_1$ and $(\Delta R_3 - n\mu_3)/\sqrt{n}\sigma_3$ converge to the random variables that obey standard normal distribution. Here, μ_1 and μ_3 represent the mean, $\mu_1 = \mu_3 = 0$, and σ_1 and σ_3 represent the standard deviation, $\sigma_1 = \sigma_3 \leq (2A_{\text{noise}})$. Taking 0.05 as the small probability even threshold and querying the standard normal distribution table, we can obtain:

$$\begin{aligned} P \left\{ \frac{\Delta R_1 - n\mu_1}{\sqrt{n}\sigma_1} \right\} &= P \left\{ \frac{\Delta R_3 - n\mu_2}{\sqrt{n}\sigma_3} \right\} = 0.05 \Rightarrow \frac{\Delta R_1 - n\mu_1}{\sqrt{n}\sigma_1} \\ &= \frac{\Delta R_3 - n\mu_3}{\sqrt{n}\sigma_3} \approx 1.65 \end{aligned} \quad (16)$$

Then, $\Delta R_1 = \Delta R_3 \leq 3.3\sqrt{n}A_{\text{noise}}$. Set $H(x) = F(x) + R(x)$, and we can obtain the following relationship:

$$\begin{aligned} & H(x + n \Delta x) - H(x) \\ &> 2 \left[n g_b - \sum_{k=0}^{n-1} f(x + k \Delta x - N_V/2 \Delta x) \right] \\ &+ [f(x + n \Delta x) - f(x)] - (9.9\sqrt{n} + 2) A_{\text{noise}} \end{aligned} \quad (17)$$

The simulation is performed to examine the distribution of sample means. Our investigation of the probability distribution of $\Delta R = R(x + n \Delta x) - R(x)$, which takes many samples from the same population, produces the statistical information shown in Table 1. Here, without loss of generality, set $x = x_{\text{vessel_center}}$, $n = N_V/4$, and $\Delta R = R(x_{\text{vessel_center}} + \frac{N_V}{4} \Delta x) - R(x_{\text{vessel_center}})$.

The probability density functions for different vessel width parameter N_V are drawn graphically and presented in Fig. 5. The statistics, including the mean value μ , standard deviation (SD) σ and sample size N_S , are given accordingly. Fig. 5 shows that the white noise CRG distribution ΔR approximates normal distribution, which shows good agreement with the central limit theorem. The effect analysis of white noise on CRG model is presented in Fig. 6.

Based on formula (17), we can increase N_V for the same vessel width (namely, increasing the image resolution) or decrease the amplitude of white noise A_{noise} to assure $H(x + n \Delta x) - H(x) > 0$ when $x \in [x_{\text{vessel_center}}, x_{\text{vessel_center}} + \delta_{\text{vessel}}/2]$ (the rest may be deduced by analogy). Of course, there is a tradeoff in the selection of image resolution. A high resolution may slow down image processing and lead to high computational complexity. Except for the unusually extreme case $\text{MAX} \left\{ R\left(x + \frac{N_V}{4} \Delta x\right) - R(x) \right\}$ (red line), the inequality $(\Delta F - \Delta R) > 0$ holds for different vessel width N_V and different percentiles P_{noise} , such as $\Delta F - \Delta R_{P1}$ and $\Delta F - \Delta R_{P3}$ (dashed lines). High levels in the scale-space representation of image will produce many local extrema

TABLE I
SIMULATION RESULTS OF WHITE NOISE CRG PROBABILITY DISTRIBUTION

		$\Delta R = R\left(x_{\text{vessel_center}} + \frac{N_V}{4} \Delta x\right) - R(x_{\text{vessel_center}})$							
Vessel width parameter N_V		$N_V=10$	$N_V=20$	$N_V=30$	$N_V=40$	$N_V=50$	$N_V=60$	$N_V=70$	$N_V=80$
Sample size N_S	valid	100000	100000	100000	100000	100000	100000	100000	100000
	missing	0	0	0	0	0	0	0	0
Maximum		8.357	13.143	17.045	16.365	21.513	22.251	22.684	27.940
Percentile (P_{noise})	0.5	-5.30699	-7.49209	-9.09509	-10.51144	-11.79207	-12.98976	-13.77376	-14.89984
	1.0	-4.80328	-6.82758	-8.20531	-9.54901	-10.63379	-11.67782	-12.57240	-13.52745
	2.5	-4.05119	-5.71832	-6.94571	-8.02848	-8.94791	-9.83107	-10.60374	-11.34800
	5.0	-3.41282	-4.80724	-5.81865	-6.76980	-7.47928	-8.30145	-8.86261	-9.59252
	95.0	3.41707	4.80741	5.86597	6.68650	7.55246	8.28209	8.96156	9.54523
	97.5	4.05674	5.69921	6.99818	7.94333	8.96311	9.82672	10.71107	11.39577
	99.0	4.77865	6.73840	8.32367	9.43396	10.62259	11.70002	12.67603	13.47419
	99.5	5.31069	7.44960	9.19152	10.39861	11.77268	12.87907	13.96489	14.83544

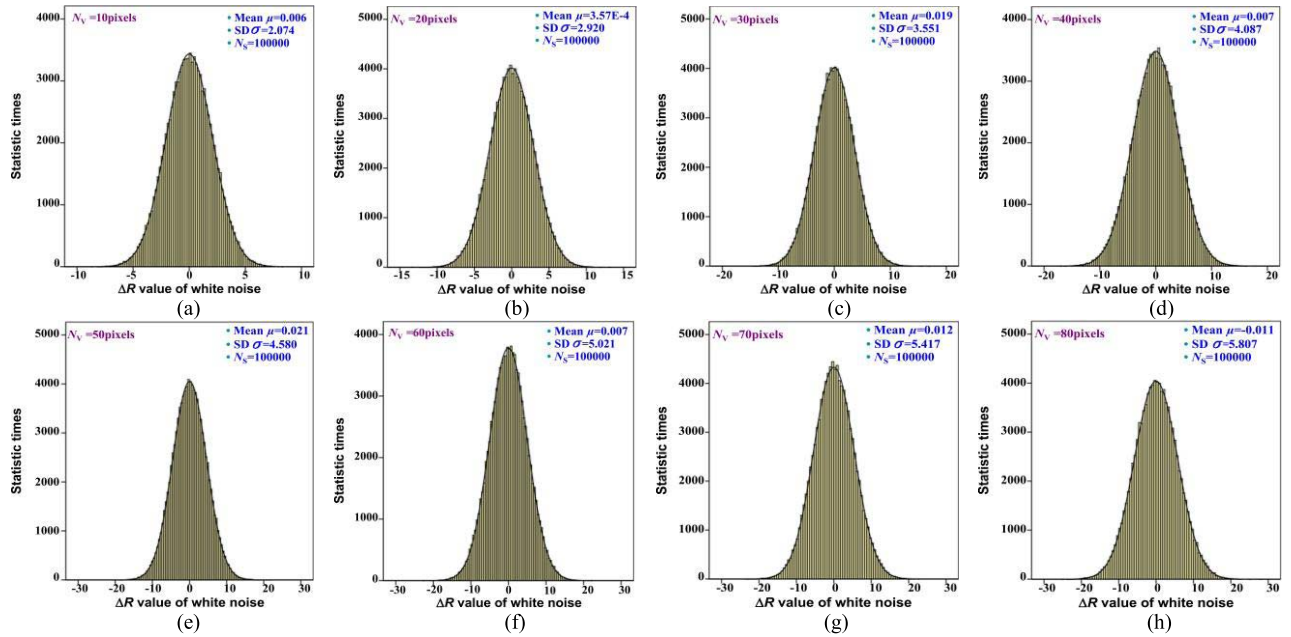


Fig. 5. Probability density function of white noise with different vessel width N_V .

that are unsuitable for featured detection, such as edges and centerline, as well as make the algorithm computationally impractical [27]. For the CRG model, the value of parameter N_V may increase with image resolution and the effect of white noise will not worsen. Fig. 6 presents that the value of $(\Delta F - \Delta R)$ increases linearly with N_V , and that the impact of white noise weakened accordingly.

Fig. 7(a) is generated to present the visual comparison between image gray and CRG models with and without white noise. The global minimum is functionally equivalent to center location, and the deviation of center position with different Noise-to-Signal ratios is shown in Fig. 7(b). Fig. 7 indicates that the CRG model is independent of white noise, and that white noise has practically no effect on the convexity and global minimum of function $F(x)$ compared with gray model $f(x)$.

D. Linear Distribution Noise Independence

Uneven illumination, color gradients, and distance gradients will cause gray changes in a NIR vessel image. Linear noise

distribution was treated as a linear curve $l(x) = mx + b$, with m and b denoting two constant coefficients, for the entire range of typical vessel widths. The CRG function $L(x)$ of linear noise $l(x)$ is expressed as follows:

$$\begin{aligned}
 L(x) &= \sum_{n=0}^{N_V/2} (l(x + n\Delta x) + l(x - n\Delta x)) \\
 &\quad - \sum_{n=N_V/2+1}^{N_V+1} (l(x + n\Delta x) + l(x - n\Delta x)) \\
 &= \left[\sum_{n=0}^{N_V/2} l(x + n\Delta x) - \sum_{n=N_V/2+1}^{N_V+1} l(x + n\Delta x) \right] \\
 &\quad + \left[\sum_{n=0}^{N_V/2} l(x - n\Delta x) - \sum_{n=N_V/2+1}^{N_V+1} l(x - n\Delta x) \right] \\
 &= L_1 + L_2
 \end{aligned} \tag{18}$$

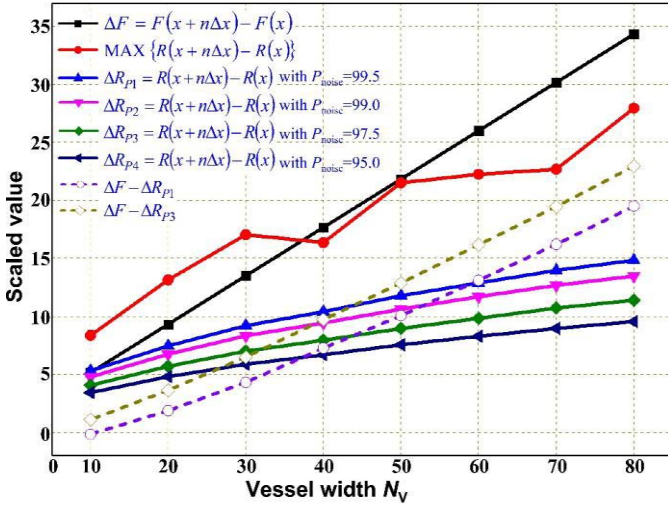


Fig. 6. Effect of white noise and image resolution on CRG model ($x = x_{\text{vessel_center}}$, $n = N_v/4$).

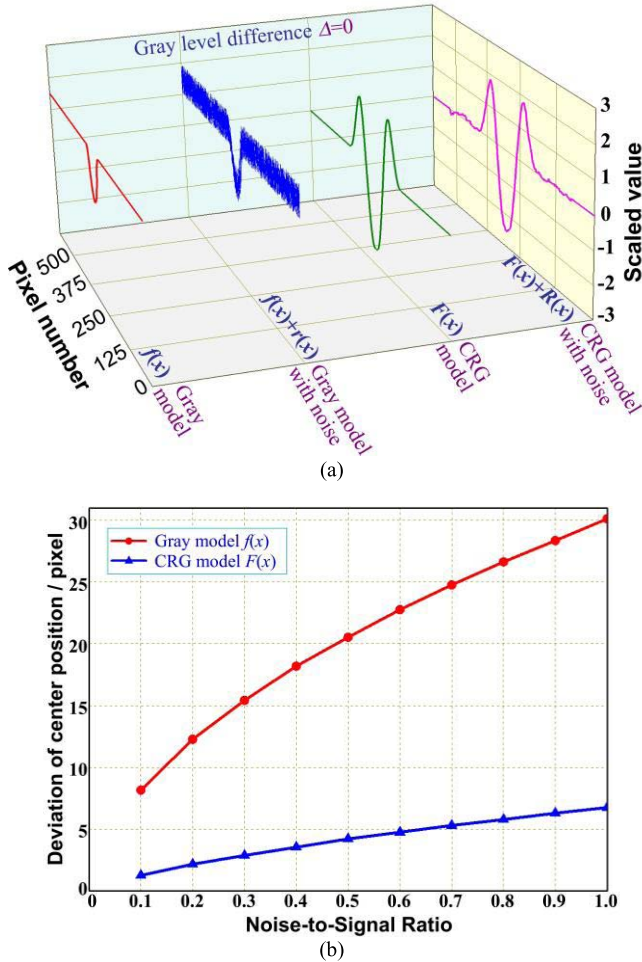


Fig. 7. Comparison between vessel gray and CRG models. (a) vessel gray and CRG models with and without white noise; (b) deviation of center position with different Noise-to-Signal ratios.

Based on the characteristics of linear function, we can obtain $|L_1| = |L_2|$, $L_1 = -L_2$. Furthermore, for any point x in vessel image, there exists:

$$L(x + n\Delta x) - L(x) = 0 \quad (n = 0, 1, 2, \dots) \quad (19)$$

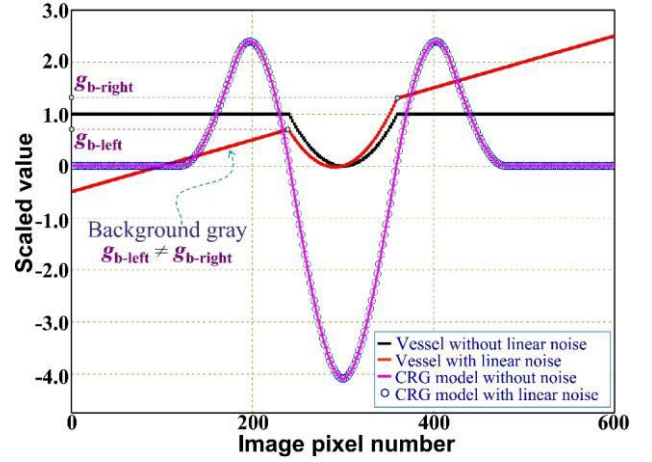


Fig. 8. Vessel gray and CRG models with and without linear noise.

The above formula (19) reveals that $L(x)$ is theoretically invariant of linear noise, and that the CRG model is independent of linear noise. The comparison between vessel gray and CRG models with and without linear noise are presented in Fig. 8. Linear noise obviously has almost no effect on the CRG model, including the global minimum F_{\min} and minimizer location.

E. Edge Location

The above discussion shows that the center position $x_{\text{vessel_center}}$ of vessels can be located with the global minimum F_{\min} . The vessel edges, which are based on the centrosymmetric vessel model, can also be extracted by synthesizing two perspectives: the center position $x_{\text{vessel_center}}$ and the equivalent width of vessel W_X . In practice, we may use the parametric variable δ_{vessel} to approximate the actual value of the vessel width W_X based on search criteria as follows:

$$\begin{cases} \delta_{\text{vessel}} < W_X \Leftrightarrow F(x_{\text{vessel_center}} \pm W_X/2) > 0 \\ \delta_{\text{vessel}} = W_X \Leftrightarrow F(x_{\text{vessel_center}} \pm W_X/2) = 0 \\ \delta_{\text{vessel}} > W_X \Leftrightarrow F(x_{\text{vessel_center}} \pm W_X/2) < 0 \end{cases} \quad (20)$$

W_X can be approximated by iteratively changing the value of parameter N_v until the single minimum is reached in the application program, as illustrated in Fig. 9(a).

In Fig. 9(a), with respect to different variable $\delta_{\text{vessel}-i}$ ($i = 1, 2, 3$), $\delta_{\text{vessel}-1} < W_X$, $\delta_{\text{vessel}-2} = W_X$, $\delta_{\text{vessel}-3} > W_X$, the values of $F(x_{\text{vessel_center}} \pm W_X/2)$ are equal to F_1 , F_2 , and F_3 , and $F_1 > 0$, $F_2 = 0$, $F_3 < 0$, respectively. The $F_{\min-i} = \min(F(x))|_{\delta_{\text{vessel}-i}}$ ($i = 1, 2, 3$) correspond to the different minima of the CRG model $F(x)$. When the equality $\delta_{\text{vessel}-2} = W_X$ holds, the function $F(x)$ has one minimizer and single minimum $F_{\min-2}$. Correspondingly, numerous minimizers (depicted with a red bold line) and minima are present under the condition $\delta_{\text{vessel}-3} > W_X$. Assume that $F'_{\min} = \min\{F'_{\min-1}, F'_{\min-2}, F'_{\min-3}\}$, then $F'_{\min-1} > F'_{\min}$, $F'_{\min-2} = F'_{\min-3} = F'_{\min}$. The CRG function $F(x)$ is a strongly and non-strictly convex function with respect to $\delta_{\text{vessel}-2} = W_X$ and $\delta_{\text{vessel}-3} > W_X$, respectively, as shown in Fig. 9(c). The convex $F(x)$ has an edge-preserving property.

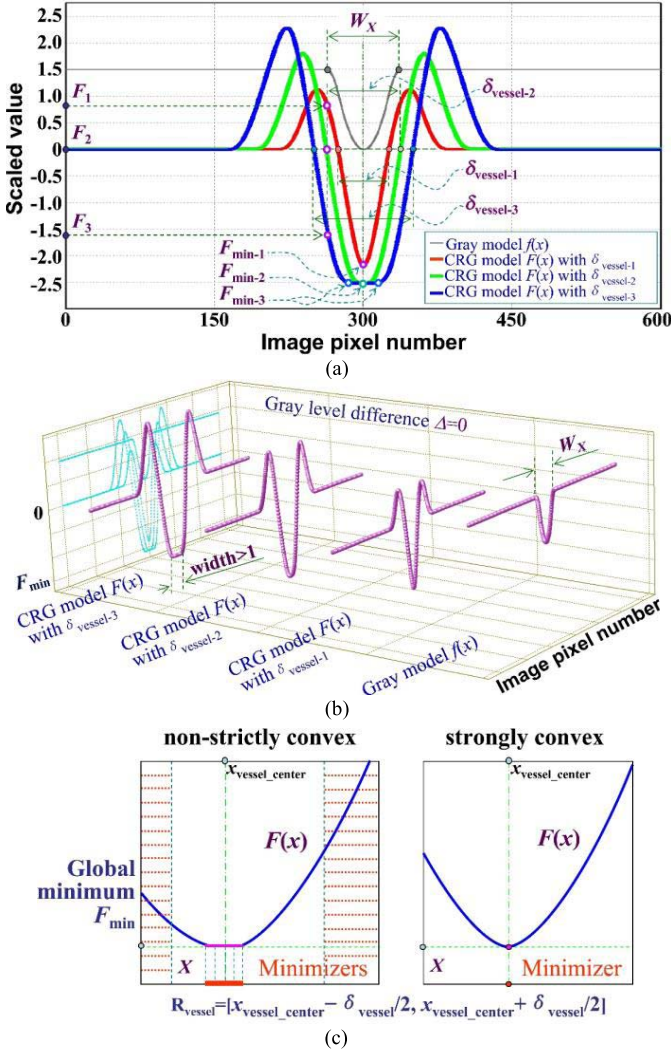


Fig. 9. Vessel edges and CRG model with different δ_{vessel} . (a) parameter-relation chart; (b) 3D sketch map; (c) convex with different width δ_{vessel} .

Thus, the issues of vessel segmentation and edge location will be transformed into the convex solution, which can be addressed with several convex optimization tools. Finally, we can locate vessel edges on the basis of the proposed CRG model and empirical approximation of parameter δ_{vessel} .

III. RESULTS

The original 600×700 pixel NIR image has 256 gray levels and is corrupted by low contrast and high noise. The CRG model and histogram equalization are compared and the results are shown in Fig. 10. The proposed CRG model obviously has a higher matching degree with human quality perception. Moreover, the vessels are easily identified from the background.

Fig. 11 presents 2D and 3D visualization maps. The 3D map presented in Fig. 11(b) shows that the vessel images in the CRG domain have better visual contrast, especially for some tiny or low contrast vessels. There is an anomaly in the upper-right corner (purple color), which resulted from non-uniform

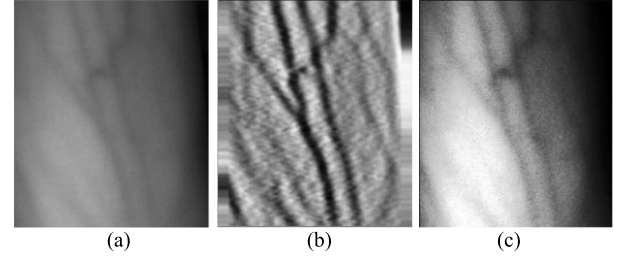


Fig. 10. Image analysis of NIR forearm image. (a) original image, (b) result of CRG model (algorithm), (c) result of histogram equalization.

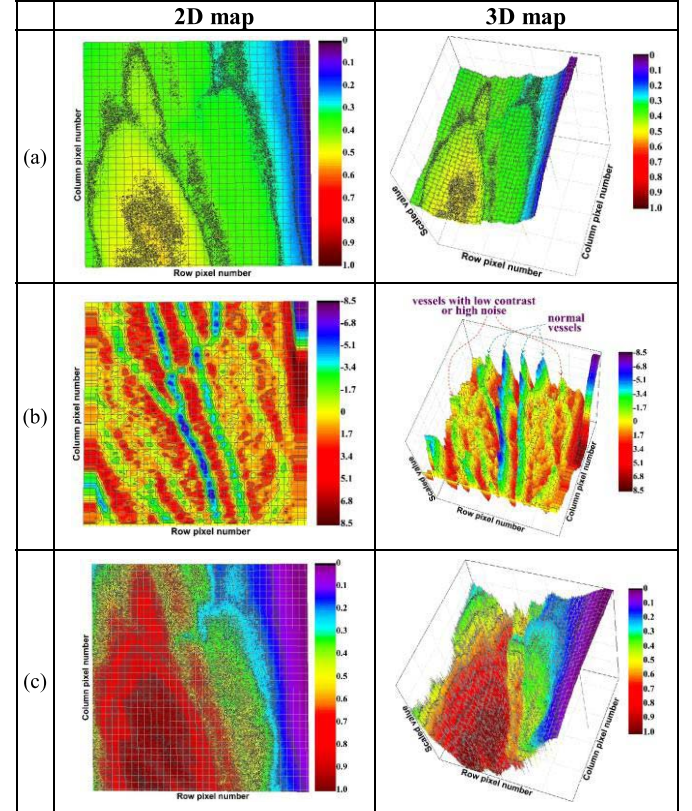


Fig. 11. 2D and 3D visualization maps of the vessel image. (a) original image; (b) results of CRG algorithm; (c) results of histogram equalization.

illumination or arm surface curvature. Selecting a region of interest (ROI) will prevent this kind of interference.

Fig. 12 presents the comparison between CRG results and adaptive binarization of histogram equalization. Vessels obtained from CRG algorithm have smoother contours and fewer outliers.

The centerline segmentation of vessels in the forearm and right hand is performed and the results are shown in Figs. 13 and 14. The traditional skeleton extraction based on iterative thinning, is chosen and applied for binarization image obtained by the adaptive histogram equalization method.

The regions with respect to bifurcations in Fig. 13 and ultra-low contrast in Fig. 14 are highlighted with red-dashed circles. The natural edges of the vessel are not degraded by the proposed algorithm. The CRG algorithm can be applied to track possible successive points of the same vessel segment or those

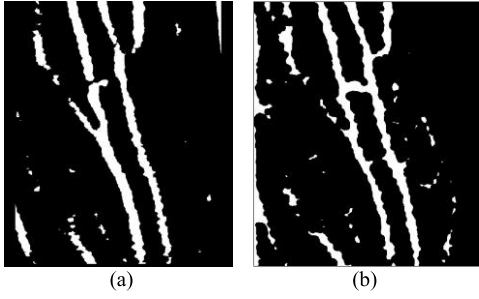


Fig. 12. The vessel edges obtained by (a) CRG algorithm and (b) adaptive binarization of histogram equalization.

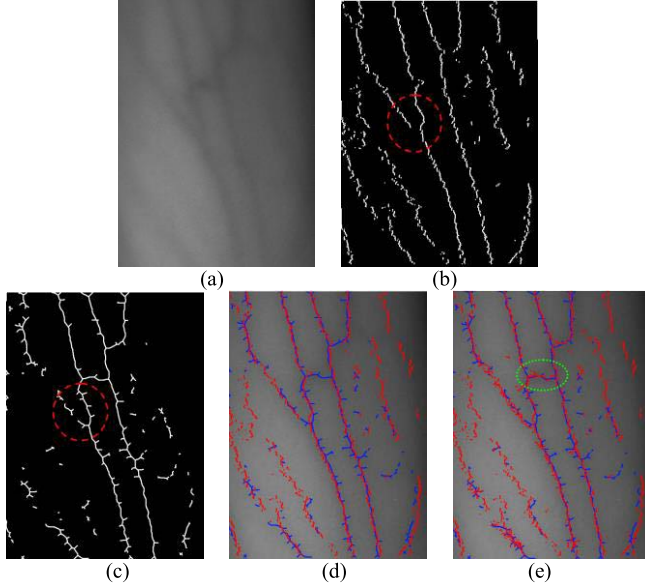


Fig. 13. Centerline segmentation of vessels in the forearm. (a) original image; (b) result from CRG model; (c) result from skeleton extraction; (d) and (e) overlapping curves from CRG (red line) and skeleton extraction (blue line) along the scanning directions (X-axis) and (Y-axis), respectively.

of its bifurcated segments without human interaction. The key aspects are the continuity and smoothness of vessel centerlines, even for branches with relatively small bifurcation angles. Moreover, the algorithm has superior enhancement compared with the traditional skeleton extraction. The results obtained from the CRG model can be used for further quantitative analysis [28] and application, such as automated venipuncture. We especially need to extract the vessel with a fairly long straight centerline for venipuncture device applications. Along different scanning directions, such as X-axis and Y-axis, Figs. 13(d) and 13(e) can be obtained, respectively. In this study, the former can significantly segment and locate vessel centerlines along the longitudinal axis of the forearm, and the latter may also be used to search vessels in the radial direction, as shown by green dotted circle in Fig. 13(e).

Noise suppression may obliterate faint objects (orange dashed circle), as shown in Figs. 14(b) and 14(c). Object regions that are fragmented by a growing region are also possible in low-SNR situations. Many different kinds of interference are present in more realistic images. These interferences may cause either over-segmentation (too much and

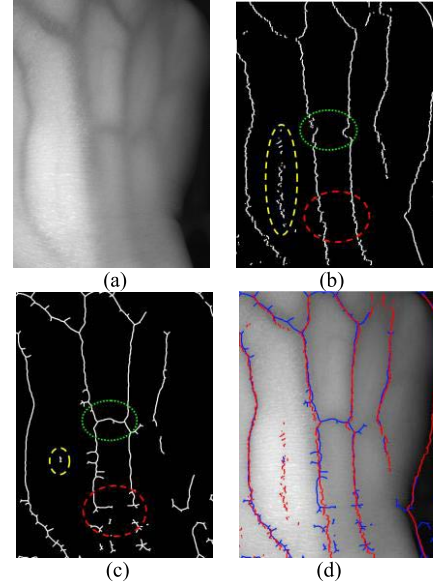


Fig. 14. Centerline segmentation of vessel in the right hand. (a) original image; (b) result from CRG model; (c) result from skeleton extraction; (d) overlapping curves from CRG (red line) and skeleton extraction (blue line).

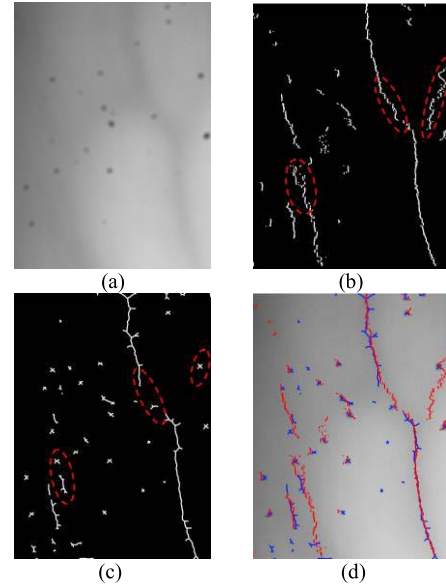


Fig. 15. Centerline segmentation of local vessel with speckle noise. (a) original image; (b) result from CRG model; (c) result from skeleton extraction; (d) overlapping curves from CRG (red line) and skeleton extraction (blue line).

small vessel regions) or under-segmentation (too less and large vessel segments). Speckle noise may originate from some diseased anatomical structures or NIR imaging systems. Noise obscures vessels in the image. The original image with ultra-low contrast and speckle noise is rendered in the algorithm performance test, as shown in Fig. 15. Regardless, the above comparison indicates that the results of CRG application are better than the traditional methods.

IV. DISCUSSION AND CONCLUSIONS

The CRG algorithm is proposed to emphasize the features of contextually related regions, including vessel size and

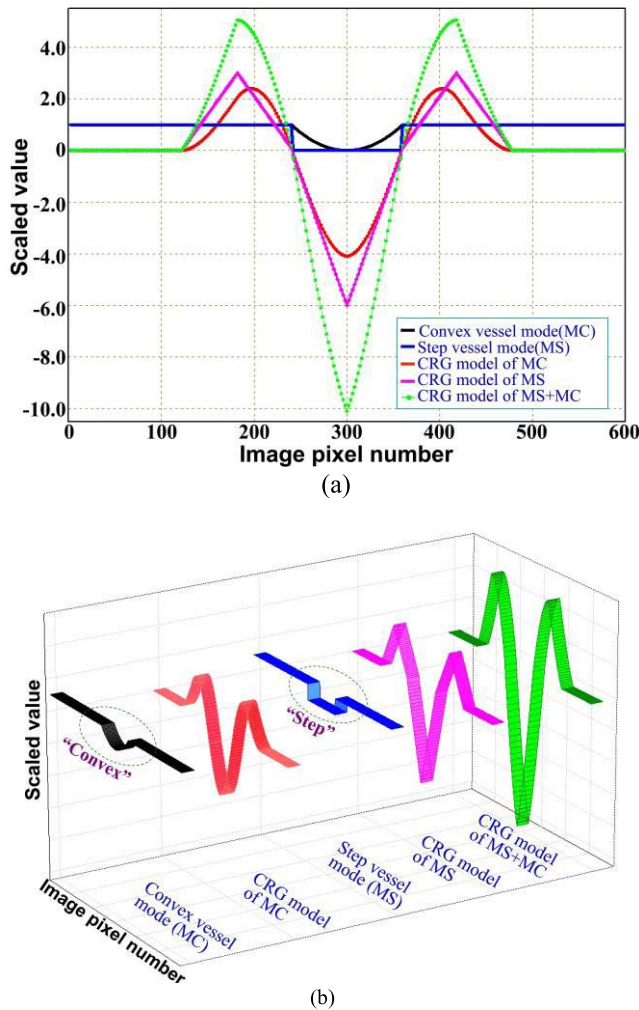


Fig. 16. Comparison between “Convex” and “Step” contour modes. (a) 2D projection; (b) 3D sketch map.

shape. A region-based gradient approach is selected for noise suppression. The CRG model decreases the number of local extrema and obtains a single global minimum for each vessel by means of convex properties.

A. Contour Mode

The cross-section profile of the vessel is approximated by a convex with a similar parabolic distribution. The global minimum is located at the centerline position of the vessel profile, and the minimizer passes through the vessel axis along the length direction. Fig. 16 presents the qualitative comparison between the results from “Convex” and “Step” contour modes. The CRG model can locate the center position of the identified object with the global minimum for two different contour modes.

In the centrosymmetric model of vessel, the gray level difference between the background and the maximal gray value of vessel is assumed to be greater than or equal to zero, $\Delta \geq 0$. Thus, the condition for inequality $\Delta > 0$ is equivalent to the superposition of two modes: “Convex” and “Step” (green ball-point line).

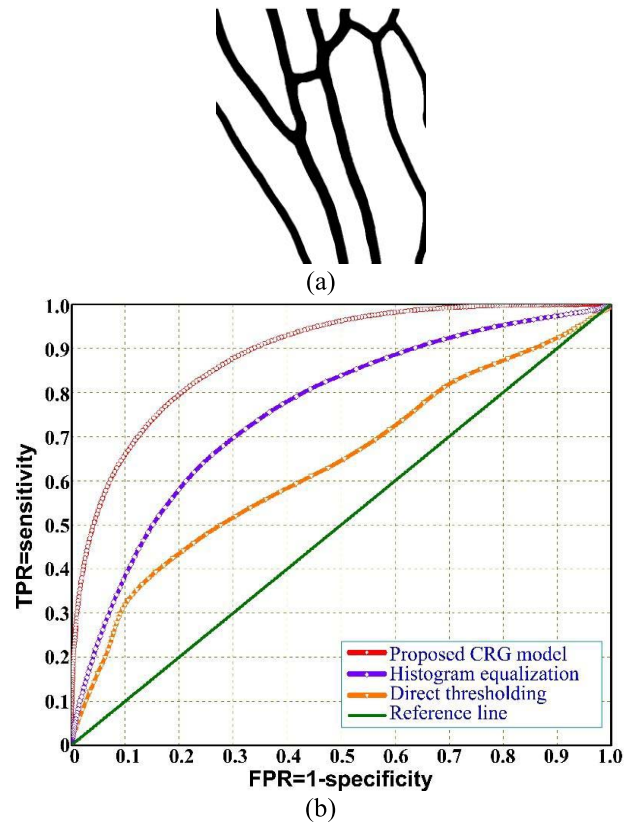


Fig. 17. ROC analysis of different methods. (a) gold standard; (b) ROC curves ($N_V = 30$).

B. ROC Analysis

Perfect segmentation is often impossible because of over-segmentation or under-segmentation. In addition to visual comparison, segmentation and location results can also be evaluated quantitatively as true positive (TP) and true negative (TN), when a pixel is correctly segmented as a vessel or non-vessel, respectively; false negative (FN), when a pixel in a vessel is segmented in the non-vessel area; and false positive (FP), when a non-vessel pixel is segmented as a vessel pixel. The most commonly used statistical measures to evaluate the performance of binary segmentation outcome are sensitivity and specificity, which are expressed as $TP/(TP + FN)$ and $TN/(TN + FP)$, respectively [29]. The reference image is a manually labeled image constructed by medical experts [30]. The estimated ROC curve depends on the true positive rate and false positive rate, with the key metric being the area under the curve (AUC). Finally, Fig. 17 presents the ROC curves of different methods produced by varying the segmentation threshold and estimating the corresponding measures. The corresponding AUC are 88.8%, 63.5%, 75.7%, and 50%.

C. Directivity and Complexity

In Figs. 14(b) and 14(c), the red dashed circles highlight striking features of continuity and smoothness with respect to vessel centerline segmentation, whereas green dotted circles accent the directivity of vessel recognition. At a general level,

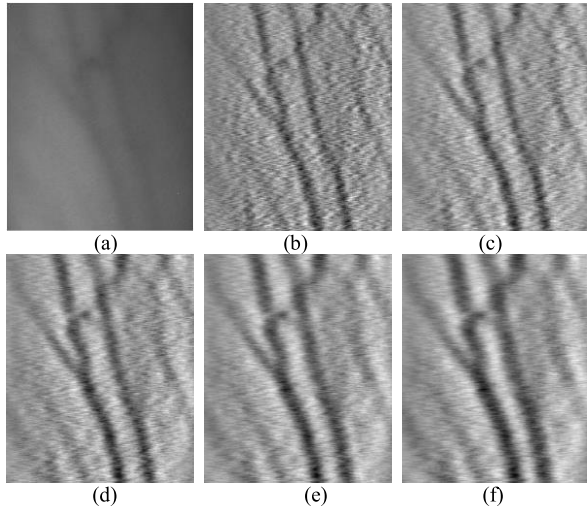


Fig. 18. Comparison with different input parameter N_V for vessels in the forearm. (a) original image, (b) 20 pixel, (c) 25 pixel, (d) 30 pixel, (e) 35 pixel, and (f) 40 pixel.

the angle of venipuncture (Fig. 1) is designed to be less than the reference value of 40° . When the venipuncture angle ψ is closed to the limitation value of 180° , the branch of the vessel has a large variation in the bifurcation angle, which is almost normal to the arm (or hand) length direction. We can adopt directional filtering techniques to obtain multidirectional search and location, as shown in Fig. 13(e). The CRG model can also be expanded in multi-neighborhood directions [31] to segment and locate vessel centerlines and edges in any direction and any width for general purposes. Direction-based approaches will reduce practicability and efficiency and increase complexity, especially for practical medical applications in terms of integration into complex venipuncture systems.

D. Parameter Initialization

N_V is used as an input parameter in the CRG model. N_V is directly related to the size of the recognized object of interest in an image, such as vessel centerline or width. Moreover, N_V represents the neighborhood region size, which has a crucial effect on the performance of the CRG algorithm. The selection of neighborhood size should be addressed for local thresholding segmentation methods. Vessel width is also a wanted parameter that is unknown *a priori*. Fig. 18 presents the comparison with different input values of N_V for vessels in the forearm. Comparative analysis based on preliminary human perception indicates that the CRG model is insensitive to quantitative changes in N_V that range from 20 to 40 pixels. Meanwhile, the quantitative comparison of the ROC values with different parameter N_V and methods is shown in Table II, and the CRG model has a mean of 0.882 (SD = 0.014). In general, the CRG model has an improved robustness with respect to parameter initialization.

For vessels in the right hand Fig. 19 presents the comparison with different input values of N_V , and the quantitative comparison of the ROC values is shown in Table III.

TABLE II
QUANTITATIVE COMPARISON WITH DIFFERENT PARAMETER N_V
AND METHODS FOR VESSELS IN THE FOREARM

CRG model	N_V	ROC Value	
	20	0.865	Mean 0.882 SD 0.014
	25	0.869	
	30	0.888	
	35	0.896	
	40	0.890	
Histogram equalization		0.755	
Direct thresholding		0.635	

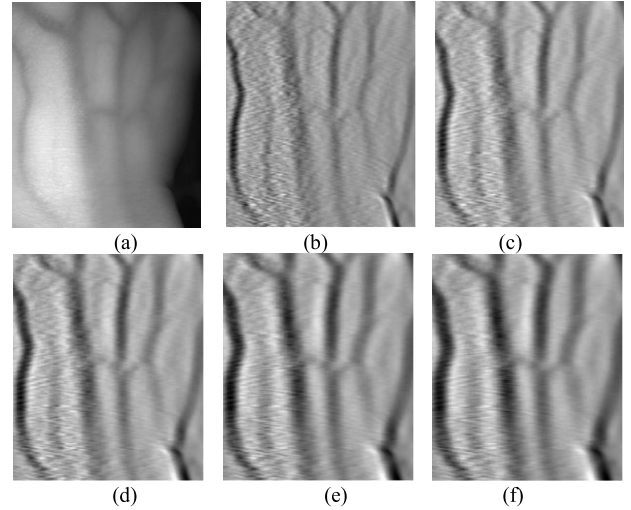


Fig. 19. Comparison with different input parameter N_V for vessels in the right hand. (a) original image, (b) 20 pixel, (c) 25 pixel, (d) 30 pixel, (e) 35 pixel, and (f) 40 pixel.

TABLE III
QUANTITATIVE COMPARISON WITH DIFFERENT PARAMETER N_V
AND METHODS FOR VESSELS IN THE RIGHT HAND

CRG model	N_V	ROC Value	
	20	0.858	Mean 0.884 SD 0.015
	25	0.890	
	30	0.896	
	35	0.892	
	40	0.884	
Histogram equalization		0.735	
Direct thresholding		0.486	

In conclusion, the main contribution of the present study is a novel CRG algorithm. This algorithm is superior to the standard histogram equalization and skeleton extraction methods, especially for addressing the continuity and smoothness of vessel centerlines. The proposed algorithm is also independent of white and linear noise. Therefore, this model is a potential powerful method for extracting vessel information for automated venipuncture systems. In future works, we will extend the application of the CRG model to ultrasonic image analysis and extraction of minute vessels in medical treatment and related diseases.

ACKNOWLEDGMENT

This research is supported by the State Key Laboratory of Precision Measurement Technology and Instruments, the National Natural Science Foundation of China (Grant No. 51275259 and No. 61362035) and the National Important Scientific Instrument Development Program of China (Grant No. 2011YQ030134).

REFERENCES

- [1] X. Hu, Y. Zhou, and Z. Wu, "A 2.5 dimensional vein imaging system for venipuncture," *Proc. SPIE*, vol. 8668, pp. 86685A-1–86685A-6, Mar. 2013.
- [2] S.-W. Jang, K.-H. Park, and G.-Y. Kim, "Skin region segmentation using an image-adapted colour model," *Int. J. Comput. Appl. Technol.*, vol. 52, nos. 2–3, pp. 142–149, 2015.
- [3] A. Shahzad, N. M. Saad, N. Walter, A. S. Malik, and F. Meriaudeau, "An efficient method for subcutaneous veins localization using Near Infrared imaging," in *Proc. 5th Int. Conf. IEEE Intell. Adv. Syst. (ICIAS)*, Jun. 2014, pp. 1–4.
- [4] Y. Zhao, L. Rada, K. Chen, S. P. Harding, and Y. Zheng, "Automated vessel segmentation using infinite perimeter active contour model with hybrid region information with application to retinal images," *IEEE Trans. Med. Imag.*, vol. 34, no. 9, pp. 1797–1807, Sep. 2015.
- [5] J. S. Duncan and N. Ayache, "Medical image analysis: Progress over two decades and the challenges ahead," *IEEE Trans. Pattern Anal. Mach. Intell.*, vol. 22, no. 1, pp. 85–105, Jan. 2000.
- [6] C. Kirbas and F. Quek, "A review of vessel extraction techniques and algorithms," *ACM Comput. Surv.*, vol. 36, no. 2, pp. 81–121, 2004.
- [7] N. Singh and L. Kaur, "A survey on blood vessel segmentation methods in retinal images," in *Proc. IEEE Int. Conf. Electron. Des. Comput. Netw. Autom. Verif. (EDCAV)*, Jan. 2015, pp. 23–28.
- [8] D. L. Pham, C. Xu, and J. L. Prince, "Current methods in medical image segmentation," *Annu. Rev. Biomed. Eng., Annu. Rev.*, vol. 2, no. 1, pp. 315–337, 2000.
- [9] M. Paulinas, D. Miniotas, M. Meilunas, and A. Ušinskas, "An algorithm for segmentation of blood vessels in images," *Elektron. Elektrotech.*, vol. 83, no. 3, pp. 25–28, 2015.
- [10] H. Li and A. Yezzi, "Vessels as 4-D curves: Global minimal 4-D paths to extract 3-D tubular surfaces and centerlines," *IEEE Trans. Med. Imag.*, vol. 26, no. 9, pp. 1213–1223, Sep. 2007.
- [11] D. G. Kang, D. C. Suh, and J. B. Ra, "Three-dimensional blood vessel quantification via centerline deformation," *IEEE Trans. Med. Imag.*, vol. 28, no. 3, pp. 405–414, Mar. 2009.
- [12] J. V. B. Soares, J. J. G. Leandro, R. M. Cesar, H. F. Jelinek, and M. J. Cree, "Retinal vessel segmentation using the 2-D Gabor wavelet and supervised classification," *IEEE Trans. Med. Imag.*, vol. 25, no. 9, pp. 1214–1222, Sep. 2006.
- [13] G. Azzopardi, N. Strisciuglio, M. Vento, and N. Petkov, "Trainable COS-FIRE filters for vessel delineation with application to retinal images," *Med. Image Anal.*, vol. 19, no. 1, pp. 46–57, Jan. 2015.
- [14] D. Marin, A. Aquino, M. E. Gegundez-Arias, and J. Bravo, "A new supervised method for blood vessel segmentation in retinal images by using gray-level and moment invariants-based features," *IEEE Trans. Med. Imag.*, vol. 30, no. 1, pp. 146–158, Jan. 2011.
- [15] J. Staal, M. D. Abramoff, M. Niemeijer, M. A. Viergever, and B. van Ginneken, "Ridge-based vessel segmentation in color images of the retina," *IEEE Trans. Med. Imag.*, vol. 23, no. 4, pp. 501–509, Apr. 2004.
- [16] E. Ricci and R. Perfetti, "Retinal blood vessel segmentation using line operators and support vector classification," *IEEE Trans. Med. Imag.*, vol. 26, no. 10, pp. 1357–1365, Oct. 2007.
- [17] O. Wink, W. J. Niessen, and M. A. Viergever, "Multiscale vessel tracking," *IEEE Trans. Med. Imag.*, vol. 23, no. 1, pp. 130–133, Jan. 2004.
- [18] Y. Yin, M. Adel, and S. Bourennane, "Retinal vessel segmentation using a probabilistic tracking method," *Pattern Recognit.*, vol. 45, no. 4, pp. 1235–1244, Apr. 2012.
- [19] Y. Chen *et al.*, "Curve-like structure extraction using minimal path propagation with backtracking," *IEEE Trans. Image Process.*, vol. 25, no. 2, pp. 988–1003, Feb. 2016.
- [20] V. Paquit, J. R. Price, F. Mériaudeau, and K. W. Tobin, "3D multispectral light propagation model for subcutaneous veins imaging," *Proc. SPIE*, vol. 6913, pp. 69130D-1–69130D-10, Mar. 2008.
- [21] Y. Chen *et al.*, "Artifact suppressed dictionary learning for low-dose CT image processing," *IEEE Trans. Med. Imag.*, vol. 33, no. 12, pp. 2271–2292, Dec. 2014.
- [22] Y. Chen *et al.*, "Improving abdomen tumor low-dose CT images using a fast dictionary learning based processing," *Phys. Med. Biol.*, vol. 58, no. 16, pp. 5803–5820, 2013.
- [23] Y. Chen *et al.*, "Improving low-dose abdominal CT images by weighted intensity averaging over large-scale neighborhoods," *Eur. J. Radiol.*, vol. 80, no. 2, pp. e42–e49, Nov. 2011.
- [24] L. Li and M. K. H. Leung, "Integrating intensity and texture differences for robust change detection," *IEEE Trans. Image Process.*, vol. 11, no. 2, pp. 105–112, Feb. 2002.
- [25] J. M. Gauch, "Image segmentation and analysis via multiscale gradient watershed hierarchies," *IEEE Trans. Image Process.*, vol. 8, no. 1, pp. 69–79, Jan. 1999.
- [26] C. Hennemersperger, M. Baust, P. Waelkens, A. Karamalis, S.-A. Ahmadi, and N. Navab, "Multi-scale tubular structure detection in ultrasound imaging," *IEEE Trans. Med. Imag.*, vol. 34, no. 1, pp. 13–26, Jan. 2015.
- [27] T. Lindeberg, "Scale-space: A framework for handling image structures at multiple scales," in *Proc. CERN School Comput.*, Egmond aan Zee, The Netherlands, 1996, pp. 8–21.
- [28] P. Zou, P. Chan, and P. Rockett, "A model-based consecutive scanline tracking method for extracting vascular networks from 2-D digital subtraction angiograms," *IEEE Trans. Med. Imag.*, vol. 28, no. 2, pp. 241–249, Feb. 2009.
- [29] M. Vlachos and E. Dermatas, "Fuzzy segmentation for finger vessel pattern extraction of infrared images," *Pattern Anal. App.*, vol. 18, no. 4, pp. 901–919, Nov. 2015.
- [30] M. E. Gegundez-Arias, A. Aquino, J. M. Bravo, and D. Marin, "A function for quality evaluation of retinal vessel segmentations," *IEEE Trans. Med. Imag.*, vol. 31, no. 2, pp. 231–239, Feb. 2012.
- [31] P. Getreuer, "Image interpolation with contour stencils," *Image Process. On Line*, vol. 1, pp. 70–82, Aug. 2011.